

## Article

## Quantitative Morphology of Epithelial Folds

Nick Štorgel,<sup>1,2</sup> Matej Krajnc,<sup>1,\*</sup> Polona Mrak,<sup>3</sup> Jasna Štrus,<sup>3</sup> and Primož Ziherl<sup>1,2,4</sup><sup>1</sup>Jožef Stefan Institute, Ljubljana, Slovenia; <sup>2</sup>Faculty of Mathematics and Physics and <sup>3</sup>Biotechnical Faculty, University of Ljubljana, Ljubljana, Slovenia; and <sup>4</sup>Erwin Schrödinger International Institute for Mathematical Physics, University of Vienna, Vienna, Austria

**ABSTRACT** The shape of spatially modulated epithelial morphologies such as villi and crypts is usually associated with the epithelium-stroma area mismatch leading to buckling. We propose an alternative mechanical model based on intraepithelial stresses generated by differential tensions of apical, lateral, and basal sides of cells as well as on the elasticity of the basement membrane. We use it to theoretically study longitudinal folds in simple epithelia and we identify four types of corrugated morphologies: compact, invaginated, evaginated, and wavy. The obtained tissue contours and thickness profiles are compared to epithelial folds observed in invertebrates and vertebrates, and for most samples, the agreement is within the estimated experimental error. Our model establishes the groove-crest modulation of tissue thickness as a morphometric parameter that can, together with the curvature profile, be used to estimate the relative differential apicobasal tension in the epithelium.

## INTRODUCTION

Many epithelial morphologies are spatially modulated rather than flat, the best-known examples being villi and crypts in the mammalian small intestine. These formations serve a specific physiological function closely related to their shape—the protruding villi increase the area for absorption of nutrients, and the recessed crypts contain glands secreting mucus and enzymes—so their shape must be robust. This applies even more to embryonic epithelia responsible for the initial development of the body plan, including key transformations such as gastrulation or neurulation.

The robustness of shape is best ensured by relying on simple biophysical processes. From the mechanical perspective, villi, crypts, and various types of epithelial folds are most straightforwardly seen as a buckling instability of a layer attached to a substrate of smaller area (1,2). Area mismatch can lead to wrinkles, creases, and ridges, as well as simple and period-doubled folds (3,4). Also possible are more complex shapes such as zig-zag and labyrinthine folds and various villus- and crypt-like morphologies (5–11). Area mismatch is usually related to the differential growth of the epithelium and the supporting tissue, which may depend on the local shape of the epithelium so as to promote either evaginated or invaginated folds (5), thereby distinguishing between villi and crypts.

The buckling theory is nontrivial but intuitive (3,12–15), yet by treating the tissue locally as a homogeneous layer, it disregards the apicobasal polarity present in all simple

epithelia. The apical, lateral, and basal domains of the cell membrane are biochemically and functionally distinct, implying that their mechanical properties must be different, too. In part, the differences can be due to the distribution of cell-adhesion molecules such as cadherins and integrins, which localize at the lateral and basal domains and render the effective surface tension of these domains smaller than that of the apical domain. This is nicely illustrated by the shape of adhering mouse embryonic cells which shows that the cell-lumen interface is less tense than the cell-cell contact zone, suggesting that adhesion decreases membrane tension (16). Another microscopic mechanism contributing to the differential effective tensions is the distinct pattern of myosin organization within the cell. For example, in *Drosophila* ovary follicle epithelium, apical myosin forms a random polygonal mesh, whereas basal myosin is arranged in parallel fibers with a more even, albeit polarized, in-plane distribution (17), so that one can distinguish between the apical constriction and the basal contraction modes. The mechanical aspects of cell apicobasal polarity can also be witnessed in the curling of *Xenopus* embryonic epithelium peeled off the inner ectoderm, as well as by the folding of explants into spherules (18) or by the formation of epithelial vesicles in *std* mutant *Drosophila* embryos (19). These spontaneous deformations are consistent with the presence of intraepithelium stresses favoring curved over flat tissue shape. Generated by actomyosin contractility, cell-cell adhesion, and other related cell-level mechanisms (16,20–22), these stresses could also be responsible for the complex epithelial morphologies.

This hypothesis is not at odds with the buckling theory, because both mechanisms may well act simultaneously, but its conceptual framework is different in several ways. First, it interprets the epithelial morphology in terms of

Submitted August 10, 2015, and accepted for publication November 12, 2015.

\*Correspondence: matej.krajnc@ijs.si

Nick Štorgel and Matej Krajnc contributed equally to this work.

Editor: Stanislav Shvartsman.

© 2016 by the Biophysical Society  
0006-3495/16/01/0269/9

<http://dx.doi.org/10.1016/j.bpj.2015.11.024>



the intrinsic preferred shape of cells and does not rely exclusively on the antagonism between the tissue and the substrate. Second, the substrate (which is still needed to ensure that the epithelium is globally planar across a large enough distance) may be liquid-like and thus free of the permanent shear stresses characteristic of the buckling theories. This is more consistent with the view that on long time-scales, supporting tissues can be remodeled in response to stress. Finally, intraepithelium forces alone combined with confinement typical for embryos of most animal species can reproduce certain morphogenetic transformations at a stage when the elastic support is absent or not well developed, e.g., during gastrulation and neurulation (23–25).

So far, the intraepithelium stress hypothesis has been explored within two related physical models. In one of them, cell shape is determined by effective surface tensions of the basal, lateral, and apical sides and cytoplasm is treated as an incompressible fluid (26). This model was used to interpret the formation of the ventral furrow in *Drosophila* as a collective process involving all of the embryo (27) and to demonstrate that the intraepithelium stresses alone can reproduce the well-developed longitudinal folds seen, e.g., in the stomach of an ascidian tunicate *Styela clava* (28). A somewhat different approach where the apical surface tension is replaced by the circumferential line tension of the actin cable was employed to interpret the bending and buckling of flat tissues, as well as the stability of epithelial spherules and tubes (29).

The theoretical fold morphologies obtained within the basic surface tension model (28) are encouraging as a proof-of-principle support of the intraepithelium stress hypothesis, but they fall short of reproducing in detail the broad spectrum of experimental observations. This suggests that although the apicobasal tension may drive folding, it is not the only force that shapes the tissues. Here, we generalize the basic model by including the basement membrane, a thin extracellular matrix composed of collagen fibers and laminins separating the epithelium from the connective tissue. Our improved theory is anatomically more faithful and provides a more definite test of the hypothesis, because it shows that the folds are stable despite the bending rigidity of the membrane. Although it partly counterbalances the intraepithelial stresses, the membrane leads to a greater variety of folds, which can be divided into four distinct types identified in various invertebrate and vertebrate epithelia. Most fold types are characterized by a pronounced groove-to-crest tissue thickness modulation, and by screening the folds using the proposed classification and measuring the modulation, one can infer the relative apical and basal tensions of cells.

## MATERIALS AND METHODS

Histological micrographs in Fig. 3, A\*\*, D\*, D\*\*, and E\*, were taken from the collection of histological sections at the Department of Biology, Biotechnical Faculty, University of Ljubljana. Sections were inspected

and imaged by light microscope Zeiss (Oberkochen, Germany) AxioImager Z.1 equipped with a HRc AxioCam camera and Axiovision software.

## Surface-tension model

Our model relies on the differential adhesion hypothesis (30), treating cells in a medium as incompressible droplets characterized by cell-cell and cell-medium surface tensions, the shape of the cell aggregate minimizing the total surface energy. In a monolayer tissue, tensions of cell-lumen, cell-cell, and cell-basement-membrane contacts can be attributed to a cell's cortex tension,  $\sigma$ , to differential tension,  $\eta$ , associated with apicobasal polarity, and to cell-cell adhesion strength,  $\gamma$  (26). Apart from the three surface terms, the tissue energy includes a term representing the elasticity of the basement membrane. Indentation experiments suggest that the membrane does behave as an isotropic solid material with a well-defined Young modulus (31), so that its low-energy deformation mode is bending just like in thin plates; we further assume that during fold formation, cells can glide on the membrane so that any stretching stresses are absent (32). In this case, we can approximate the elastic energy of the membrane by the Kirchhoff-Love theory (33), which for parallel straight folds reduces to  $W_{\text{bend}} = (K_{\text{bend}}/2) \int C_{\text{bend}}^2 dA$ . Here,  $K_{\text{bend}}$  and  $C_{\text{bend}}$  are the bending rigidity and the local curvature of the membrane, respectively, and the integral goes over its area. This continuum model describes the bending elasticity of the membrane; other aspects of its mechanical behavior, such as stress-induced rearrangement of the network of fibers forming the membrane, are more easily included in agent-based models (34,35).

The total energy of the model epithelium and the basement membrane studied here thus reads

$$W = \sigma(A_a + A_b + A_l) + \eta(A_b - A_a) - \frac{\gamma}{2} A_l + W_{\text{bend}}, \quad (1)$$

where  $A_a$ ,  $A_b$ , and  $A_l$  are the sums of surface areas of the apical, basal, and lateral cell sides, respectively. As  $\sigma$ ,  $\eta$ , and  $\gamma$  cannot be measured directly, we turn to an equivalent representation that involves the effective tensions of the different cell sides—the apical, basal, and lateral tension of  $\Gamma_a = \sigma - \eta$ ,  $\Gamma_b = \sigma + \eta$ , and  $\Gamma_l = 2\sigma - \gamma$ , respectively. In all the results presented here, apical tension is the same in all cells, as are basal and lateral tension.

Much as most models of epithelial in-plane structure are reduced to its en face view (36), folds and related morphologies are usually studied by considering the representative tissue cross section (37). We too resort to this simplification to expose the mechanisms at work and to dispose of tissue topology, which is subdominant in this context. The approximation made is controlled in that it replaces the true scaling of cell side area with cell volume by that derived for the cross section, and it does not affect the relative apical and basal surface energies responsible for fold formation.

Here, the tissue cross section (Fig. 1 A) is represented by a chain of quadrilateral cells with straight edges supported by a basement membrane of local curvature  $C_{\text{bend}}$  (Fig. 1, B and C). By assuming that the dimension of cells along the folds is constant, the fixed-cell-volume constraint is translated into a fixed-area constraint for the quadrilaterals ( $A = \text{const.}$ ). The characteristic length scale is then  $\sqrt{A}$  and the energy per unit length along the folds is expressed in units of  $\Gamma_l \sqrt{A}$ . Using the reduced apical and basal tensions, as well as the reduced bending modulus of the basement membrane, defined by

$$\alpha = \frac{\Gamma_a}{\Gamma_l}, \beta = \frac{\Gamma_b}{\Gamma_l}, \text{ and } \kappa = \frac{K_{\text{bend}}}{\Gamma_l A}, \quad (2)$$

respectively, the dimensionless tissue energy reads

$$w = \alpha l_a + \beta l_b + \frac{1}{2} l_l + \frac{\kappa}{2} \int c_{\text{bend}}^2 ds. \quad (3)$$

Here  $l_a$ ,  $l_b$ , and  $l_l$  are sums of the reduced apical, basal, and lateral edge lengths, respectively, measured in units of  $\sqrt{A}$ ;  $c_{\text{bend}} = C_{\text{bend}}\sqrt{A}$  is the dimensionless curvature of the basement membrane and the integral goes along the membrane contour.

The equilibrium cross sections of the model epithelium are obtained by numerically minimizing the energy (Eq. 3) at given  $\alpha$ ,  $\beta$ , and  $\kappa$  using periodic boundary conditions to enforce the global planarity of epithelium, varying the wavelength of the fold and the number of cells in it. This is done within the Surface Evolver package (38), and the contour of the basement membrane is discretized such that it coincides with the basal sides of cells. Our code also includes a routine that prevents cell-cell overlap by mimicking hard-core repulsion between nonneighboring cells (Section S1 in the Supporting Material).

## RESULTS

**Fig. 1 D** shows the phase diagram at fixed reduced apical tension  $\alpha = 0.6$  in the regime where the reduced basal tension is large enough so that the preferred shape of cells is basally constricted and thus wedge-shaped. Not all cells in the epithelium can assume the preferred shape because of the bending rigidity of the basal membrane and because of the substrate-enforced global planar nature of the tissue. Nonetheless, the total energy of the fold morphology is energetically favorable compared to the flat epithelium provided that the magnitude of the differential tension is neither too small nor too large (28) (Section S1). As a result, intraepithelial stresses do lead to compact, invaginated, evaginated, and wavy fold morphologies, described below and illustrated by characteristic waveforms in points C1, I1, E, and W, respectively, in **Fig. 1 D**; a more detailed discussion

of fold shapes is presented in Section S2. At fixed reduced basal tension  $\beta = 0.6$ , we find somewhat different variants of compact and invaginated folds (waveforms C2 and I2 in **Fig. 1 E**), but evaginated and wavy folds are absent.

### Compact folds

This type of epithelium is stable at large enough differential tension and small basement-membrane bending modulus. In this regime, a large fraction of cells in the waveform undergo constriction and are tall; in waveform C1 in **Fig. 1 D**, the basally constricted cells form the crest and face the lumen. On the other hand, the groove consists of short trapezoidal cells. Contours of the epithelium-lumen interface and of the basement membrane are both notched. Compact folds differ from the other fold morphologies in wavelength and amplitude, which are both comparable to cell size; in waveform C1, they are about twice the average cell height. Note that many cells on the opposite sides of the groove are pushed against each other, showing that this repulsion, too, shapes the waveform. In fact, as basal tension is increased at fixed bending modulus, this effect prevails over the bending rigidity of the basement membrane (Section S1).

At large apical and small basal tension, compact folds consist of tall apically constricted cells forming the groove and less numerous short cells forming the crest (waveform C2 in **Fig. 1 E**), yet the overall shape of the tightly packed waveform is rather similar to that at large  $\beta$  and small  $\alpha$ .

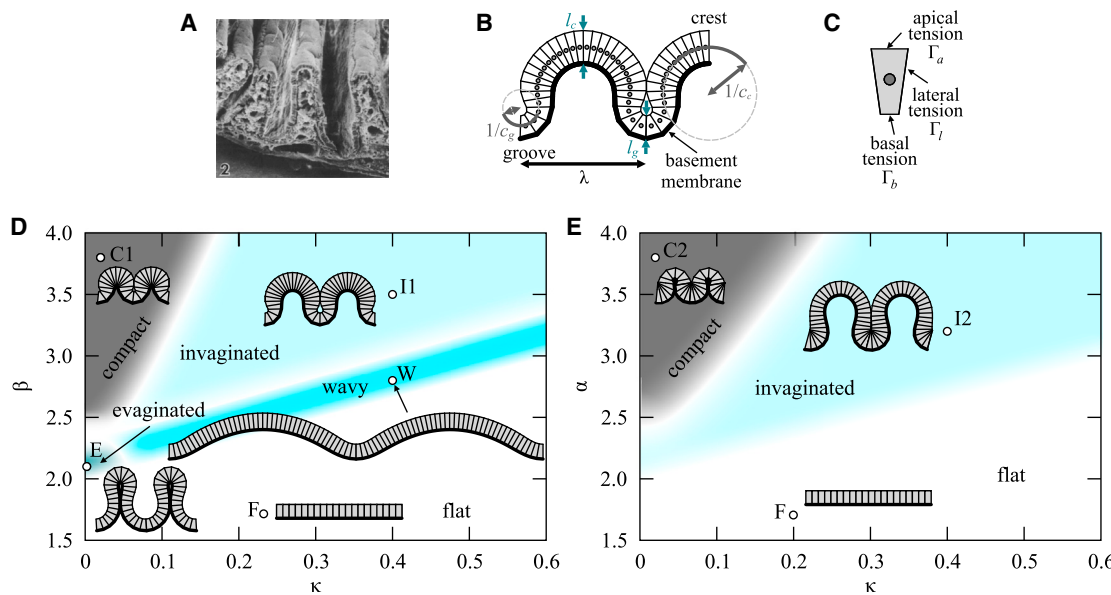


**FIGURE 1** Longitudinal folds in the gastric epithelium of *Styela clava* (**A**; reproduced with permission of Integrative and Comparative Biology from Ermak (44)). (**B**) The model cross section, showing groove and crest curvatures,  $c_g$  and  $c_c$ , respectively, and fold wavelength  $\lambda$ ; also plotted is the basement membrane (thick black line). (**C**) The preferred cell shape is determined by the relative tensions of the apical, lateral, and basal sides. (**D** and **E**) Phase diagrams of the fold morphologies for the fixed-apical-tension case in the  $(\kappa, \beta > \alpha = 0.6)$  plane (**D**) and the fixed-basal-tension case in the  $(\kappa, \alpha > \beta = 0.6)$  plane (**E**), showing compact, invaginated, evaginated, and wavy folds. The color shading shows the regions of the phase diagram where the different fold morphologies are stable. The boundaries between these regions are guides to the eye. To see this figure in color, go online.

## Invaginated folds

At large differential tension and large membrane bending modulus, the fold waveform is marked by deep closed grooves and broad crests. The main qualitative difference compared to the compact folds is that in the invaginated morphology, the contour of the basement membrane is undulating rather than notched. In turn, this means that the invaginated folds have a wavelength and amplitude considerably larger than cell height. The amplitude and thus the depth of the groove can be increased either by increasing the bending modulus or by decreasing tissue differential tension (Section S1).

As in compact folds, there exist two invaginated variants. In the  $\beta > \alpha$  variant (waveform I1 in Fig. 1 D), cells in the crest are taller than those in the groove, which also means that the  $180^\circ$  turn in the groove contains fewer cells than the crest. The  $\alpha > \beta$  variant represented by waveform I2 in Fig. 1 E is exactly the opposite: short cells/thin tissue in the crest and tall cells/thick tissue in the grooves.

## Evaginated folds

At basal tension larger than the apical tension but not too big, the epithelium forms evaginated folds with broad grooves and narrow yet tall crests (waveform E in Fig. 1 D). In many ways, this morphology is the diametrical opposite of the invaginated folds: in the former, the tissue baseline is at the groove level and crests are best viewed as fins extending into the lumen, whereas the latter have a baseline at the crest level and grooves protruding into the substrate.

In evaginated folds, modulation of tissue thickness along the waveform is small. Crests become more round with increasing bending modulus, eventually leading to meandering waveforms with enhanced crest-groove symmetry (Section S2). There only exists the  $\beta > \alpha$  variant of evaginated folds.

## Wavy folds

This morphology is found at intermediate basal tensions  $\beta > \alpha$  and is characterized by a wavelength much larger than cell height (waveform W in Fig. 1 D). With a flat-crest/sharp-groove shape, wavy folds are generally quite the opposite of the cnoidal water waves; yet there also exist variants with a symmetric, sine-like contour (Section S2). Tissue thickness hardly varies along the waveform.

## Thickness and curvature profiles

The geometrical features of the four fold types are best captured by profiles of tissue thickness (i.e., cell height),  $l$ , and curvature,  $c$ , along the waveform. Both quantities are best presented relative to fold wavelength,  $\lambda$ , and Fig. 2

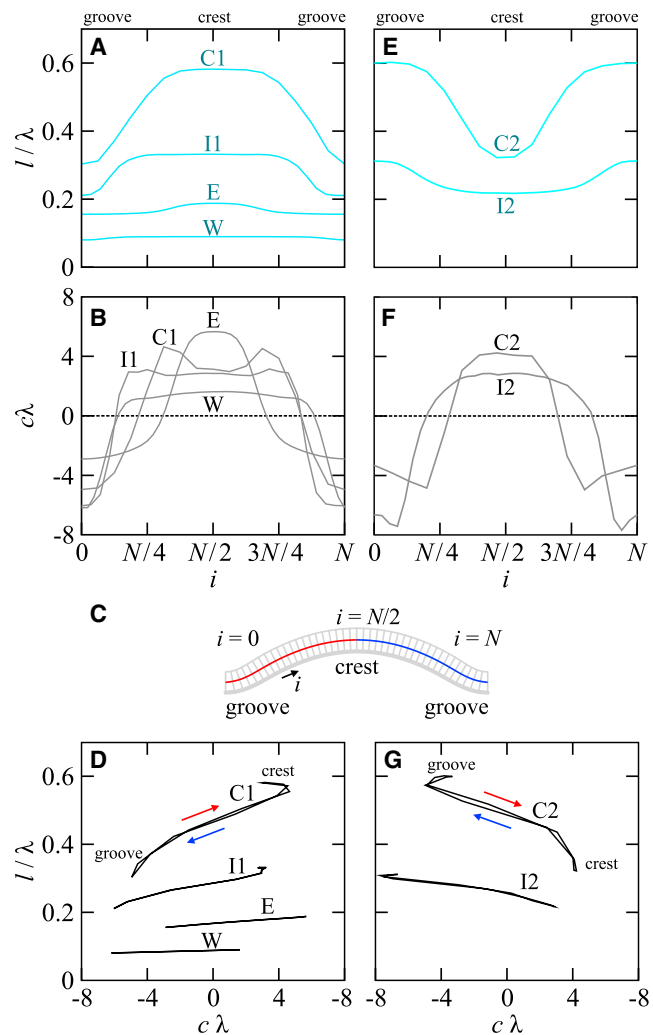


**FIGURE 2** Epithelial thickness and curvature profiles of the four representative  $\beta > \alpha = 0.6$  folds from Fig. 1 D (A and B) and for the two  $\alpha > \beta = 0.6$  folds from Fig. 1 E (E and F); cell index  $i = 0$  and  $N$  in the groove and  $i = N/2$  in the crest (C). In all cases, the step-like variation of thickness coincides with the transition from the groove domain with a negative curvature to the crest domain with a positive curvature; this is clearly visible in (E) and (F), where the different sizes of the crest domains in waveforms C2 and I2 are readily seen in both thickness and curvature profiles. (D) and (G) show tissue thickness versus curvature for folds from Fig. 1, D and E, respectively. In this representation, the left end of each curve corresponds to the groove (where  $i = 0$  and  $N$ ) and the right end represents the crest (where  $i = N/2$ ). The steady increase of thickness with curvature in waveforms in (D) is a signature of a positive correlation of these two quantities, and the steady decrease of those in (G) indicates that they are anticorrelated. Switchbacks at the tops of curves C1, I1, C2, and I2 are due to cell-cell repulsion which affects the packing of cells in compact and invaginated folds. In all images, thickness and curvature are scaled by fold wavelength  $\lambda$ . To see this figure in color, go online.

shows  $l/\lambda$  and  $c\lambda$  in the six examples from Fig. 1, D and E, plotted against cell index,  $i$ .  $N$  is the number of cells in the waveform and  $i = 0$  is the lowest cell in a groove. In our discrete model, this cell may be slightly displaced from the bottom of the contour viewed as a smooth curve, so that the profiles are not perfectly symmetric about  $i = N/2$ .

Finally, the plots are neither perfectly smooth nor perfectly symmetric due to the rather small number of cells in a waveform, typically between 15 and 45 depending on fold type. This artifact of the discrete model used mostly affects the curvature profiles (Fig. 2, B and F), because the local curvature is calculated from the position of the geometric centers of three neighboring cells. In the segments of waveform with a very low number of cells per unit length, this approximation for the local curvature is quite rough.

The most remarkable result seen in Fig. 2 is the large modulation of the tissue thickness in compact and invaginated folds. In the former, the largest thickness of the waveform is almost 200% of the smallest thickness (Fig. 2, A and E, C1 and C2), and in the latter this ratio is  $\sim 150\%$ . On the other hand, the thicknesses of evaginated and wavy folds are virtually uniform.

As per the reduced curvature,  $c\lambda$  (Fig. 2, B and F), its alternating sign on going from the groove to the crest and to the next groove is of course expected, but the step-like profile seen in all fold morphologies is not. In turn, the sharp boundaries between the domains of positive and negative curvature imply that the ratio of the groove and crest curvatures,  $-c_g/c_c$  (Fig. 1 B), can be used to identify a given fold type based on easily measurable quantities.

By comparing the thickness and curvature profiles for a given fold type in Fig. 2, A and B, we find that they are correlated in the sense that the maximal and the minimal thickness coincide with maximal and minimal curvature, respectively. On the other hand, those in Fig. 2, E and F, are anticorrelated. This effect is clearly seen in Fig. 2, D and G, where tissue thickness is plotted against curvature, the cell index running along each loop (the loops appear degenerated because the waveforms are almost perfectly symmetric). The thickness-curvature coupling is more prominent in compact and invaginated folds of either type but not in the evaginated and wavy folds, where tissue thickness does not vary much along the waveform. By comparing the parameters of these waveforms, we conclude that the nature of coupling is determined by the sign of the differential tension (correlation for  $\alpha - \beta < 0$  and anticorrelation for  $\alpha - \beta > 0$ ), whereas its magnitude increases with  $|\alpha - \beta|$  and decreases with  $\kappa$ ; also important is cell-cell repulsion, which stabilizes the shape of most waveforms.

Although the four fold types are very distinct, the shape of the waveform changes continuously across the phase diagram (Fig. S8), and there exists no order parameter that could be used to precisely define the transitions between them. Thus, we resort to suitable auxiliary criteria to partition the phase space. For example, in the invaginated folds, the apical sides of some nonneighboring cells touch, but in the wavy folds, they do not due to the larger bending rigidity of the basement membrane, and so the invaginated-wavy transition can be associated with the point of detachment. Even though the thus-introduced boundaries between the fold morphologies in Fig. 1, D and E, are semiquantitative,

they suggest that compact, invaginated, and flat morphologies are rather robust in the sense that they occupy a considerable part of the phase diagram, whereas evaginated and wavy folds are more restricted. Qualitatively, we may conclude that 1) the compact folds are stable at large differential tensions,  $|\alpha - \beta|$ , and small basement-membrane bending moduli; 2) the invaginated folds are stabilized by a moderate bending modulus; and 3) the evaginated and wavy folds require that the basal tension be larger than the apical tension, but not very dramatically, and evaginated folds additionally rely on a flexible basement membrane.

In Fig. 1, D and E, we zoom into the part of the diagram where the differential tension,  $|\alpha - \beta|$ , is large enough to stabilize fold morphologies but still realistically moderate; the global topology of the phase diagram is discussed in Section S2. Finally, by changing tissue lateral tension defined by  $\alpha + \beta$  (28) the results presented above can be readily adapted to describe columnar as well as cuboidal epithelia. Our results also provide an explanation of why squamous fold morphologies are rarely observed. Folds do require a certain minimal magnitude of the differential tension,  $|\alpha - \beta| \geq 1.4$  (Section S1), and given that both  $\alpha$  and  $\beta$  are positive, this implies that  $\alpha + \beta$  must also be  $> 1.4$ . In this regime, cells are cuboidal or columnar rather than squamous.

## DISCUSSION

### Classification of observed fold morphologies

All four types of epithelial folds were identified in histological sections of invertebrate and vertebrate tissues reported in the literature or imaged in our laboratory. Compact  $\beta > \alpha$  folds are present in the wing imaginal disc of *Drosophila* larva (Fig. 3 A\*) and in parts of cat lung bronchus (Fig. 3 A\*\*). Examples of invaginated  $\alpha > \beta$  folds include intestinal epithelium of bony fishes (silver sailfin molly *Poecilia latipinna* (Fig. 3 B\*)) and the epithelium of mammalian colon (rat small intestine (Fig. 3 B\*\*)). The invaginated  $\beta > \alpha$  folds are seen in cnidarian actinopharynx (*metridium* (Fig. 3 C\*)), and in vertebrate bronchiole (cow and mouse (Fig. 3, C\*\* and C\*\*\*)), where wavy folds are present, too (mouse (Fig. 3 D\*\*\*)). Wavy morphology is also found in the body surface of snail *Helix* sp. (Fig. 3 D\*) and in the hindgut of earthworm *Lumbricus* sp. (Fig. 3 D\*\*). The evaginated epithelium is identified in cat lung bronchiole (Fig. 3 E\*), in monkey oviduct (Fig. 3 E\*\*), and in trout intestine (Fig. 3 E\*\*\*). Additional physiological details are summarized in Section S3.

Each micrograph in Fig. 3 is combined with a theoretical waveform that fits the fold morphology in question, represented by individual cells if their boundaries are visible in the micrograph or by the contours if cell boundaries cannot be easily seen. The quantitative agreement of both large and fine features is quite good, despite the inherent fold-to-fold

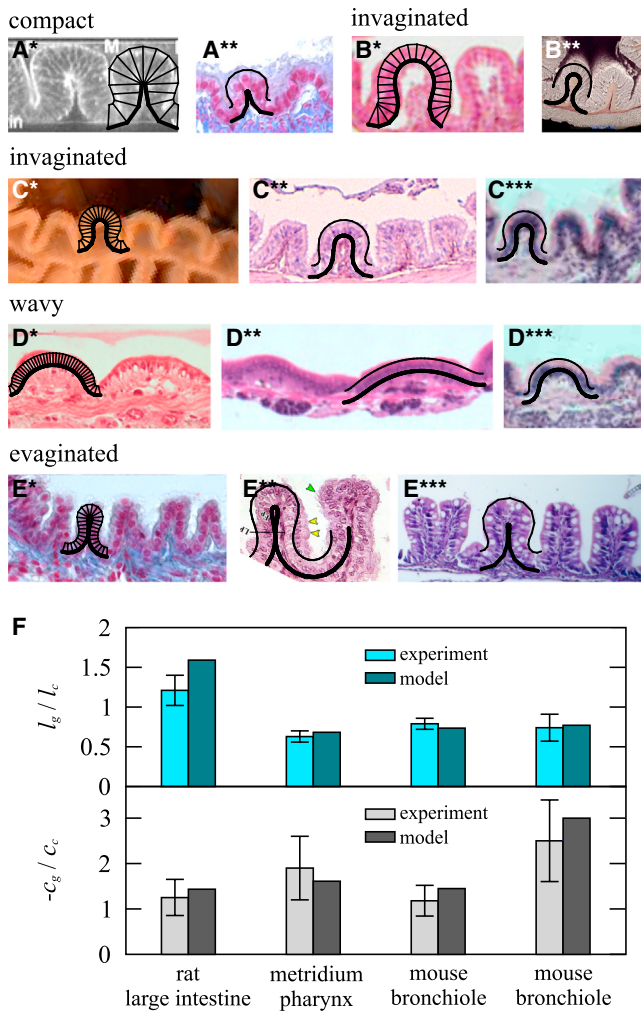


FIGURE 3 Examples of the four fold morphologies in vertebrates and invertebrates. Compact folds ( $A^*$  and  $A^{**}$ ), invaginated folds with  $\alpha > \beta$  ( $B^*$  and  $B^{**}$ ) and  $\beta > \alpha$  ( $C^*$ – $C^{***}$ ), wavy folds ( $D^*$ – $D^{***}$ ), and evaginated folds ( $E^*$ – $E^{***}$ ). ( $A^*$ ) is reproduced from Johnstone and Wells (45), published under Creative Commons license CC-BY; ( $B^*$ ) is reproduced with permission of the International Journal of Zoological Research from Mobarak and Sharaf (46); ( $B^{**}$ ) is reproduced with permission from Visuals Unlimited (<http://visualsunlimited.photoshelter.com/gallery-image/Dr-Richard-Kessel/G00002iBlh8co7x8/I0000m18wfK0VDHU/C0000eOTVcBEMmt>); ( $C^*$ ) is courtesy of M. Ford and J. Houseman (University of Ottawa; [http://salinella.bio.uottawa.ca/BIO2135/labs/default.php?PoftheP/2012/Lab03/Lab03\\_Cnid.htm](http://salinella.bio.uottawa.ca/BIO2135/labs/default.php?PoftheP/2012/Lab03/Lab03_Cnid.htm)); ( $C^{**}$ ) is courtesy of P. W. L. Kwan (Tufts University School of Medicine; <http://ocw.tufts.edu/Content/4/coursehome/221120/221123>); ( $C^{***}$ ) and ( $D^{***}$ ) are courtesy of K. Perryman-Snow (<http://www.calpoly.edu/~eperryma/yewang/Home.htm>); ( $E^{**}$ ) and ( $E^{***}$ ) are courtesy of M. Moyal (Hebrew University of Jerusalem; <http://courses.md.huji.ac.il/histology/female/XIII-5.html>) and A. Ortiz (Norel Animal Nutrition), respectively. Micrographs ( $A^{**}$ ), ( $D^*$ ), ( $D^{**}$ ), and ( $E^*$ ) were taken in our laboratory. ( $F$ ) Comparison of experimental and theoretical relative groove/crest tissue thickness and curvature in the folds from ( $B^{**}$ ), ( $C^*$ ), ( $C^{***}$ ), and ( $D^{***}$ ) (left to right). The parameter values of model folds that describe the experimental data ( $A^*$ – $E^{***}$ ) are listed in Table S1. To see this figure in color, go online.

variability natural in soft tissues and despite several methodological disadvantages. In particular, histological sections are usually not cut exactly perpendicular to the epithelial sheet nor to the folds, so the fold shape may appear distorted in various ways (Section S4); moreover, in real tissues cells are usually not strictly perpendicular to the contour of the epithelium, as theoretically predicted. Second, cell borders often cannot be precisely determined due to the limited resolution of the microscope and due to the presence of extracellular material near cell surfaces. Lastly, our model does not include several biological processes that too can affect epithelial shape, especially the presence of two or more cell populations in the tissue, cell division, and external forces due to muscle activity.

### Epithelial morphometry

Despite these impediments, the quantitative comparison of theoretical and experimental fold shapes in Fig. 3,  $A^*$ – $E^{***}$ , is convincing. Here, we present the relative groove/crest tissue thickness,  $l_g/l_c$ , and curvature,  $-c_g/c_c$ , as the most easily measurable features of the waveforms. In view of the well-defined step-like thickness and curvature profiles, their groove/crest variation can be considered representative of a given waveform, although in a dedicated experiment, one would ideally compare the whole contour. Fig. 3 F shows these two ratios in epithelia in the rat small intestine (Fig. 3  $B^{**}$ ), in metridium actinopharynx (Fig. 3  $C^*$ ), and in mouse bronchiole (Fig. 3,  $C^{***}$  and  $D^{***}$ ). In each image, tissue thickness and curvature were measured in the fold overlaid with the theoretical waveform, and error bars were determined by the inaccuracy of the cell border and the radii of curvature. The agreement found is good in all four cases, calling for further experimental studies permitting an in-depth morphometric analysis of samples with many waveforms.

Based on the measured values of  $l_g/l_c$  and  $-c_g/c_c$ , as well as on the overall shape of waveforms, we can roughly estimate the reduced differential tension and the reduced bending rigidity of the basement membrane of these epithelia (Section S5). In rat small intestine in Fig. 3  $B^{**}$ ,  $\alpha - \beta = 3.2$  and  $\kappa = 0.4$ ; in metridium actinopharynx in Fig. 3  $C^*$ ,  $\alpha - \beta = -2.2$  and  $\kappa = 0.14$ , whereas in mouse bronchiole in Fig. 3  $C^{***}$ ,  $\alpha - \beta = -1.9$  and  $\kappa = 0.1$  and in that in Fig. 3  $D^{***}$ ,  $\alpha - \beta = -2.2$  and  $\kappa = 0.3$ . Since we computed the minimal-energy shapes with a finite step in the model parameters (Section S2), the accuracy of these estimates is ~20%, which is approximately the largest relative difference between two neighboring sets of parameters used in our computations.

The shape of the different epithelial folds formed during tissue development, differentiation, and performance depends on their function. Since any single epithelium usually simultaneously serves diverse purposes, it is difficult to establish a one-to-one correspondence between a

given function and a particular epithelial type. Nonetheless, in the examples collected in Fig. 3, such relations are indicated. Compact folds may be primarily associated with reducing the length of the sheet to minimize the area occupied by epithelial cells and allow occasional dilatations or further growth (e.g., in embryos). Absorptive and secretory epithelial folds consist of invaginated or evaginated sheets with crests and grooves of various dimensions. In absorptive epithelia, crests are composed of either flattened or elongated cells with enlarged apical surface, which is consistent with the  $\alpha > \beta$  variant of the invaginated fold morphology. Cells in the grooves are apically constricted, resulting in an increased cell height. On the other hand, in secretory epithelia, the crest cells are basally constricted and apically enlarged due to the intense secretion of fluids and mucus, and the grooves of epithelia are often widely open, i.e., their radius of curvature is large enough compared to wavelength so that non-neighboring cells in the region between the groove and the crest do not touch. Transportive epithelia may have wavy, invaginated, or evaginated fold morphologies with grooves of variable depths and widths, the folds enabling lumen distension for efficient transport of air and liquids in the grooves.

At this juncture, it is worthwhile comparing the fin-like shape of longitudinal folds with villi, finger-like protrusions into the lumen typical for mammalian small intestine. Villi that are closely spaced have a considerably larger excess surface area compared to folds, and thus a superior capacity for the absorption of nutrients. However, folded epithelia are more readily stretched or compressed in the direction perpendicular to the folds, thereby better accommodating changes in size of stroma and lumen distension due to external forces exerted, e.g., by surrounding muscles. In addition, these morphologies must have a very anisotropic bending rigidity much like common corrugated paper or even insect wings (39), their resistance to bending along folds being increased. Thus, the folded epithelia may well provide some structural support, which could be relevant in neutrally buoyant animals without a skeleton, like cnidaria. In addition, evaginated folds most probably bend less compared to villi of similar dimensions when fluids flow past them. This may well increase the volume and the residence time of the fluid trapped within the grooves, enhancing the retention capacity of the folds and contributing to more efficient adsorption. These ideas are related to elastic deformations of fold morphologies, which can be readily explored in a suitably extended version of our model.

A generalization is also needed to reproduce the evaginated longitudinal folds in the stomach of *Styela clava* (Fig. 12 of (40)), which are longer than in any waveform predicted here. The discrepancy is not surprising, because gastrointestinal epithelia are known to consist of two or more physically distinct cell populations, and by describing

each population by a different set of apical, lateral, and basal tensions it should be possible to improve agreement. This is most straightforwardly done by separating 1) a groove population with an increased apical tension from 2) a crest population with an increased basal tension by 3) an intervening population of cells without a differential apicobasal tension. Within such a model, fold shape could be tuned by adjusting the size of each cell population and its three effective tensions. It is conceivable that the postulated tension gradients along the waveform are associated with cell maturation and migration toward the crest, where they are shed (40). In a similar fashion, one could seek an explanation for the alternative major and minor folds seen in the stomach of *Ciona intestinalis* (Fig. 2 E of Ermak (41)).

### Comparison to other theories

Each of our theoretical waveforms is characterized by a contour and a tissue thickness profile, and it is natural to ask whether the types of shapes reported here can be expected in other models. The existence of the folds themselves has been so far associated primarily with the area mismatch between the epithelium and the supporting stroma, typically due to certain dynamical processes within the epithelium, such as cell division and cell death (5–9). In the area-mismatch theory, the groove-crest asymmetry seen in shapes in Fig. 1 may be caused by the elasticity of the stroma at large deformations simply because the local displacement field immediately below the crest is not the mirror image of that below the grooves. This effect could well be enhanced by a suitable nonlinear elastic theory of the stroma, as well as by a curvature-dependent cell division rate (5) or an inhomogeneous preferred curvature of the basement membrane, which can be adjusted to control the shape of the waveform (34). Whether the ensuing asymmetry of the folds is as pronounced as in our waveforms, and whether the fold types generated by area mismatch agree with those proposed here, remains an open question to be resolved numerically. Alternatively, tissue buckling may be triggered by differential mechanical properties of cells, which could be efficiently implemented within a nonplanar vertex model representing the apical sides (42,43), where deformation can be caused by a suitable pattern of, e.g., cell-cell tension. One of the advantages of this approach is that it allows one to more straightforwardly include cell rearrangements, which is probably important in the formation of crypts and villi for topological reasons.

In turn, the nonplanar vertex model does not address the tissue thickness, and in the area-mismatch theory, thickness is fixed. Although the specific buckling scenarios discussed above can in principle produce contours similar to our waveforms, it is more difficult to see how they could give rise to the distinct tissue thickness profiles, some of which are quite

pronounced, as shown in Fig. 2, A and E. This previously overlooked morphometric feature can be used to estimate the intracellular tensions, as well as to compare the different models to experimental data. Fig. 4 illustrates the difference between folds generated by area mismatch and by intraepithelial stress. Fig. 4 A shows an epithelium at  $\alpha - \beta = 0$  that is buckled because of confinement mimicking competition between tissue growth and restoring elastic forces (5). Here, thickness does not vary along the tissue. The waveform in Fig. 4 B corresponds to the same epithelium additionally supported by a very rigid basement membrane with  $\kappa = 2$ , which does lead to slightly nonuniform thickness varying over a range of 1% of the average. The bottom waveform (Fig. 4 C) is our invaginated morphology with a finite apicobasal differential tension leading to a very pronounced thickness modulation with a range of about 30%. Based on such differences, one can distinguish between the possible mechanisms at work, provided, of course, that cells in the tissue can be assumed to be mechanically identical.

## CONCLUSIONS

The agreement of theoretical and experimental fold morphologies reported here supports the intraepithelial stress hypothesis, suggesting that cell-level forces and cell-cell adhesion may well be directly responsible for the observed morphologies. This view complements the area-mismatch theories where the corrugated shape of epithelia is attributed to tissue growth and cell division. The theoretical waveforms obtained allowed us to distinguish between four types of folds, and we wish that the proposed classification were

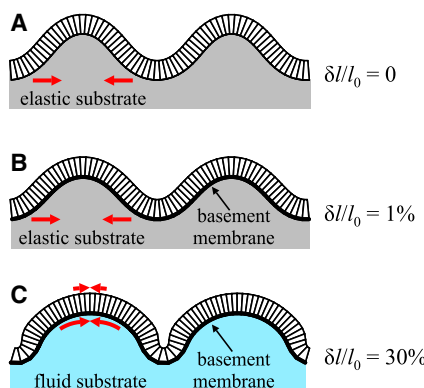


**FIGURE 4** Comparison of fold morphologies in growing tissue characterized by area mismatch (A) (no basement membrane,  $\alpha = \beta = 1.9$ ) and (B) (basement membrane of  $\kappa = 2$  included)) and in an invaginated epithelium with a finite apicobasal differential tension (C) ( $\alpha = 0.6$ ,  $\beta = 3.2$ , and  $\kappa = 0.6$ ); the parameters were chosen so that the wavelength and number of cells per fold are similar to those in (A) and (B). The relative percentages of thickness modulation are 0, 1%, and 30%, respectively. Arrows indicate that folds in (A) and (B) are stabilized by area mismatch and the elasticity of stroma, whereas that in (C) is due to apicobasal differential tension. To see this figure in color, go online.

further elaborated. Our model also predicts fold morphologies in columnar and cuboidal, but not in squamous, epithelia which is consistent with most experimental data and implies that the rare cases of folded squamous epithelial tissues should be generated by an alternative mechanism and not by apicobasal tension.

There are several ways of improving our theory. First, a three-dimensional implementation of the model should be able to reproduce zig-zag folds with a characteristic fishbone in-plane pattern (8), as well as villi and crypt morphologies, where the intraepithelial stresses are expected to play an even more important role for purely geometrical reasons (28). Second, the model can be readily extended to pseudosтратified epithelia, say, by including a finite-sized nucleus, which could be located either at the apical or at the basal side in very tall cells. The disposition of nuclei can be both the origin and the result of tissue deformation, and we expect that the phase diagram of this extended model should contain more fold waveforms than the current version. Third, our ideas may be generalized by including cell division and cell death as two mechanisms controlling buckling within the area-mismatch theory, which could well give rise to an even more diverse spectrum of waveforms (5). We are hopeful that the theoretical predictions available will stimulate further detailed morphometric studies of the various epithelial morphologies, leading to a quantitative understanding of the mechanics involved.

## SUPPORTING MATERIAL

Supporting Materials and Methods, eleven figures, and one table are available at [http://www.biophysj.org/biophysj/supplemental/S0006-3495\(15\)01205-9](http://www.biophysj.org/biophysj/supplemental/S0006-3495(15)01205-9).

## AUTHOR CONTRIBUTIONS

P.Z. designed research; N.Š., M.K., P.M., and J.Š. performed research; N.Š., M.K., P.M., J.Š., and P.Z. wrote the manuscript.

## ACKNOWLEDGMENTS

We thank P.-F. Lenne, G. Tkačik, and R. Winklbauer for stimulating discussions and J. Houseman, P. W. L. Kwan, M. Moyal, A. Ortiz, and K. Perryman-Snow for providing us with the micrographs used in Fig. 3.

This work was supported by the Slovenian Research Agency through grants P1-0184 and P1-0055, the Marie-Sklodowska-Curie European Training Network COLLDENSE (H2020-MSCA-ITN-2014 Grant No. 642774), and the European Science Foundation Research Networking Programme QuanTissue.

## REFERENCES

1. Bowden, N., S. Brittain, ..., G. M. Whitesides. 1998. Spontaneous formation of ordered structures in thin films of metals supported on an elastomeric polymer. *Nature*. 393:146–149.

2. Genzer, J., and J. Groenewold. 2006. Soft matter with hard skin: From skin wrinkles to templating and material characterization. *Soft Matter*. 2:310–323.
3. Brau, F., H. Vandeparre, ..., P. Damman. 2010. Multiple-length-scale elastic instability mimics parametric resonance of nonlinear oscillators. *Nat. Phys.* 7:56–60.
4. Wang, Q., and X. Zhao. 2015. A three-dimensional phase diagram of growth-induced surface instabilities. *Sci. Rep.* 5:8887.
5. Hannezo, E., J. Prost, and J. F. Joanny. 2011. Instabilities of monolayered epithelia: shape and structure of villi and crypts. *Phys. Rev. Lett.* 107:078104.
6. Ciarletta, P., and M. Ben Amar. 2012. Pattern formation in fiber-reinforced tubular tissues: folding and segmentation during epithelial growth. *J. Mech. Phys. Solids*. 60:525–537.
7. Ben Amar, M., and F. Jia. 2013. Anisotropic growth shapes intestinal tissues during embryogenesis. *Proc. Natl. Acad. Sci. USA*. 110:10525–10530.
8. Shyer, A. E., T. Tallinen, ..., L. Mahadevan. 2013. Villification: how the gut gets its villi. *Science*. 342:212–218.
9. Ciarletta, P., V. Balbi, and E. Kuhl. 2014. Pattern selection in growing tubular tissues. *Phys. Rev. Lett.* 113:248101.
10. Ferri, S., L. C. U. Junqueira, ..., L. O. Medeiros. 1976. Gross, microscopic and ultrastructural study of the intestinal tube of *Xenodon merremii* Wagler, 1824 (Ophidia). *J. Anat.* 121:291–301.
11. McAvoy, J. W., and K. E. Dixon. 1978. Cell specialization in the small intestinal epithelium of adult *Xenopus laevis*: structural aspects. *J. Anat.* 125:155–169.
12. Drasdo, D. 2000. Buckling instabilities of one-layered growing tissues. *Phys. Rev. Lett.* 84:4244–4247.
13. Kim, P., M. Abkarian, and H. A. Stone. 2011. Hierarchical folding of elastic membranes under biaxial compressive stress. *Nat. Mater.* 10:952–957.
14. Hohlfeld, E., and L. Mahadevan. 2011. Unfolding the sulcus. *Phys. Rev. Lett.* 106:105702.
15. Li, B., Y. P. Cao, ..., H. Gao. 2012. Mechanics of morphological instabilities and surface wrinkling in soft materials: a review. *Soft Matter*. 8:5728–5745.
16. Lecuit, T., and P. F. Lenne. 2007. Cell surface mechanics and the control of cell shape, tissue patterns and morphogenesis. *Nat. Rev. Mol. Cell Biol.* 8:633–644.
17. He, L., X. Wang, ..., D. J. Montell. 2010. Tissue elongation requires oscillating contractions of a basal actomyosin network. *Nat. Cell Biol.* 12:1133–1142.
18. Luu, O., R. David, ..., R. Winklbauer. 2011. Large-scale mechanical properties of *Xenopus* embryonic epithelium. *Proc. Natl. Acad. Sci. USA*. 108:4000–4005.
19. Tepass, U., and E. Knust. 1993. *crumbs* and *stardust* act in a genetic pathway that controls the organization of epithelia in *Drosophila melanogaster*. *Dev. Biol.* 159:311–326.
20. Dawes-Hoang, R. E., K. M. Parmar, ..., E. F. Wieschaus. 2005. Folded gastrulation, cell shape change and the control of myosin localization. *Development*. 132:4165–4178.
21. Mammoto, T., and D. E. Ingber. 2010. Mechanical control of tissue and organ development. *Development*. 137:1407–1420.
22. Martin, A. C., M. Gelbart, ..., E. F. Wieschaus. 2010. Integration of contractile forces during tissue invagination. *J. Cell Biol.* 188:735–749.
23. Lewis, W. H. 1947. Mechanics of invagination. *Anat. Rec.* 97:139–156.
24. Leptin, M. 2005. Gastrulation movements: the logic and the nuts and bolts. *Dev. Cell.* 8:305–320.
25. Rauzi, M., A. Hočevá Brezavšček, ..., M. Leptin. 2013. Physical models of mesoderm invagination in *Drosophila* embryo. *Biophys. J.* 105:3–10.
26. Derganc, J., S. Svetina, and B. Žekš. 2009. Equilibrium mechanics of monolayered epithelium. *J. Theor. Biol.* 260:333–339.
27. Hočevá Brezavšček, A., M. Rauzi, ..., P. Zíherl. 2012. A model of epithelial invagination driven by collective mechanics of identical cells. *Biophys. J.* 103:1069–1077.
28. Krajnc, M., N. Štorgel, ..., P. Zíherl. 2013. A tension-based model of flat and corrugated simple epithelia. *Soft Matter*. 9:8368–8377.
29. Hannezo, E., J. Prost, and J. F. Joanny. 2014. Theory of epithelial sheet morphology in three dimensions. *Proc. Natl. Acad. Sci. USA*. 111:27–32.
30. Steinberg, M. S. 1963. Reconstruction of tissues by dissociated cells. Some morphogenetic tissue movements and the sorting out of embryonic cells may have a common explanation. *Science*. 141:401–408.
31. Candiello, J., M. Balasubramani, ..., H. Lin. 2007. Biomechanical properties of native basement membranes. *FEBS J.* 274:2897–2908.
32. Ilina, O., and P. Friedl. 2009. Mechanisms of collective cell migration at a glance. *J. Cell Sci.* 122:3203–3208.
33. Landau, L. D., and E. M. Lifshitz. 1986. Theory of Elasticity. Pergamon Press, Oxford, United Kingdom.
34. Dunn, S.-J., A. G. Fletcher, ..., J. M. Osborne. 2012. Modelling the role of the basement membrane beneath a growing epithelial monolayer. *J. Theor. Biol.* 298:82–91.
35. D'Antonio, G., P. Macklin, and L. Preziosi. 2013. An agent-based model for elasto-plastic mechanical interactions between cells, basement membrane and extracellular matrix. *Math. Biosci. Eng.* 10:75–101.
36. Farhadifar, R., J. C. Röper, ..., F. Jülicher. 2007. The influence of cell mechanics, cell-cell interactions, and proliferation on epithelial packing. *Curr. Biol.* 17:2095–2104.
37. Odell, G. M., G. Oster, ..., B. Burnside. 1981. The mechanical basis of morphogenesis. I. Epithelial folding and invagination. *Dev. Biol.* 85:446–462.
38. Brakke, K. 1992. The Surface Evolver. *Exp. Math.* 1:145–165.
39. Rees, C. J. C. 1975. Form and function in corrugated insect wings. *Nature*. 256:200–203.
40. Ermak, T. H. 1975. Cell proliferation in the digestive tract of *Styela clava* (Urochordata: Ascidiacea) as revealed by autoradiography with tritiated thymidine. *J. Exp. Zool.* 194:449–466.
41. Ermak, T. H. 1981. A comparison of cell proliferation patterns in the digestive tract of ascidians. *J. Exp. Zool.* 217:325–339.
42. Osterfield, M., X. Du, ..., S. Y. Shvartsman. 2013. Three-dimensional epithelial morphogenesis in the developing *Drosophila* egg. *Dev. Cell.* 24:400–410.
43. Murisic, N., V. Hakim, ..., B. Audoly. 2015. From discrete to continuum models of three-dimensional deformations in epithelial sheets. *Biophys. J.* 109:154–163.
44. Ermak, T. H. 1982. The renewing cell populations of ascidians. *Am. Zool.* 22:795–805.
45. Johnstone, K., R. E. Wells, ..., M. P. Zeidler. 2013. Localised JAK/STAT pathway activation is required for *Drosophila* wing hinge development. *PLoS One*. 8:e65076.
46. Mobarak, Y. M. S., and M. M. Sharaf. 2011. Lead acetate-induced histopathological changes in the gills and digestive system of silver sailfin molly (*Poecilia latipinna*). *Int. J. Zoolog. Res.* 7:1–18.

# Quantitative morphology of epithelial folds

## Supplementary information

Nick Štorgel,<sup>†‡</sup> Matej Krajnc,<sup>†</sup> Polona Mrak,<sup>§</sup> Jasna Štrus,<sup>§</sup> and Primož Ziherl<sup>†‡¶</sup>

<sup>†</sup>Jožef Stefan Institute, Jamova 39, SI-1000 Ljubljana, Slovenia

<sup>‡</sup>Faculty of Mathematics and Physics, University of Ljubljana, Jadranska 19, SI-1000 Ljubljana, Slovenia

<sup>§</sup>Biotechnical Faculty, University of Ljubljana, Jamnikarjeva 101, SI-1000 Ljubljana, Slovenia and

<sup>¶</sup>Erwin Schrödinger International Institute for Mathematical Physics,

University of Vienna, Boltzmanngasse 9, A-1090 Vienna, Austria

## I. MECHANICAL BASIS OF FOLD FORMATION

To illustrate the various mechanisms that determine the equilibrium shape of tissues within our model (tissue lateral tension, tissue differential tension, bending rigidity of the basement membrane, cell-cell repulsion, and confinement by the stroma), it is instructive to study a free-standing 2D epithelium supported by the basement membrane alone. Unlike our main model, here the substrate enforcing a global planar geometry is absent, and all cells adopt the same shape. Thus the curvature of the chain of cells is constant but generally nonzero such that the model tissue may be either flat or curved, depending on the values of parameters.

In the dimensionless form of our discrete model (Eq. 3 of the main text), the energy of a cell attached to the basement membrane can be written as

$$w = \alpha l_a + \beta l_b + \frac{1}{2} l_l + \frac{\kappa}{2} c_{\text{bend}}^2 l_b, \quad (1)$$

where  $l_a$ ,  $l_b$ , and  $l_l$  are the lengths of apical, basal, and lateral cell sides, respectively, and  $c_{\text{bend}}$  is the curvature of the basement membrane. The lengths  $l_a$ ,  $l_b$ , and  $l_l$  are not independent because cells are incompressible and so their area is constant and normalized to 1. Instead of using these three lengths, it is convenient to parametrize cell shape by midline curvature  $c$  and height  $l$  (also representing tissue thickness) as two independent parameters (Fig. S1); cell width is then determined by the fixed-area constraint. Within this parametrization the dimensionless energy of a single cell in a free-standing epithelium–basement membrane system reads

$$w = \frac{\alpha + \beta}{l} + \frac{(\alpha - \beta)c}{2} + l \sqrt{1 + \left(\frac{c}{2l}\right)^2} + \frac{\kappa c^2}{l(2 - cl)}. \quad (2)$$

At any given reduced apical tension, basal tension, and basement membrane bending modulus ( $\alpha$ ,  $\beta$ , and  $\kappa$ , respectively) the optimal, minimal-energy cell shape is found by solving  $\partial w/\partial c = 0$ ,  $\partial w/\partial l = 0$ , which generally has to be done numerically.

Based on rectangular cells, our model is an approximation as the exact shape of a droplet-like cell carrying surface energy alone is curved like in a cluster of soap bubbles. By disregarding the curvature of the sides, we approximate the force balance at the cell-cell contact.

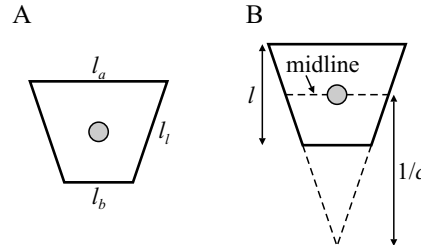


Fig. S1. Two equivalent parametrizations of cell shape: Edge-length representation based on  $(l_a, l_b, l_l)$  together with the incompressibility constraint  $A = 1$  (panel A) or curvature-height representation based on  $(c, l)$  (panel B).

Nonetheless, assuming that cell sides are flat is reasonable because our model (Eq. 1 of the main text) is to be viewed as an effective description designed so as to reproduce the overall behavior of epithelial cells, which are rarely curved, and the flat-side constraint is a part of the phenomenological framework.

Below we analyze the influence of model parameters  $\alpha$ ,  $\beta$ , and  $\kappa$  on the minimal-energy shape of the tissue.

### A. Tissue lateral tension

Cell width-to-height ratio is governed by the lateral tension defined by  $\alpha + \beta$ . In case of a flat epithelium where  $l_a = l_b$  and thus  $c = 0$  cell proportions can be calculated straightforwardly. The energy per cell is

$$w_{\text{flat}} = \frac{\alpha + \beta}{l} + l, \quad (3)$$

and the optimal cell height is determined by  $\partial w_{\text{flat}}/\partial l = 0$ . By taking into account the incompressibility constraint  $A = l_a l = 1$ , we find

$$\frac{l_a}{l} = \frac{1}{\alpha + \beta}. \quad (4)$$

$l_a/l \ll 1$  and  $l_a/l \gg 1$  correspond to a columnar and a squamous epithelium, respectively; in a cuboidal epithelium  $l_a/l \approx 1$  (Fig. S2A). Cell width-to-height ratio  $l_a/l$  also depends on tissue differential tension  $\alpha - \beta$  but this effect is subdominant compared to the interplay of tissue lateral tension  $\alpha + \beta$  and incompressibility leading

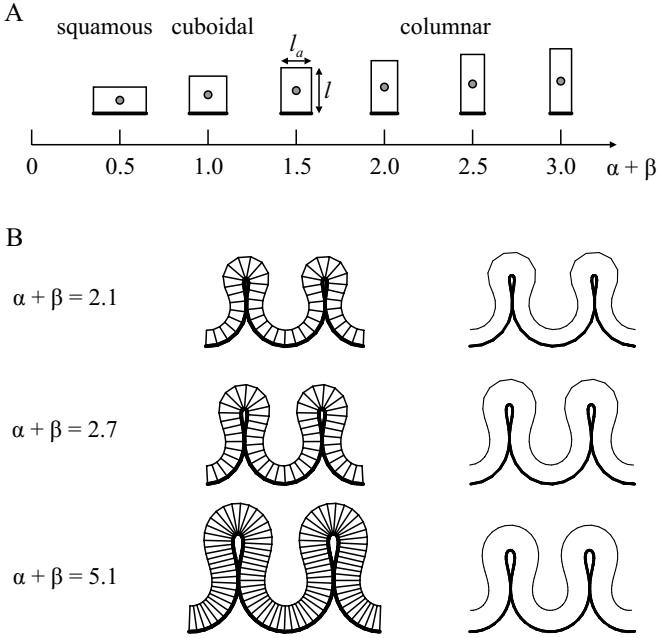


Fig. S2. Equilibrium cell shapes vs. reduced tissue lateral tension  $\alpha + \beta$  at vanishing differential tension  $\alpha - \beta$  (panel A). At small  $\alpha + \beta \ll 1$  the cell is flattened, i.e., squamous, at  $\alpha + \beta = 1$  it is isometric, i.e., cuboidal, whereas at large  $\alpha + \beta \gg 1$  it is tall, i.e., columnar. Three examples of evaginated folds with identical differential tension of  $\alpha - \beta = 1.5$  and bending rigidity  $\kappa = 0.001$  and different tissue lateral tensions  $\alpha + \beta$  (panel B, left column). In the right column, the folds are scaled such that their wavelengths are identical, which emphasizes that their shapes are very similar.

to Eq. 4, which is a rather good estimate of  $l_a/l$  for all nontrivial folded structures studied here.

Cell width-to-height ratio  $l_a/l$  also affects the equilibrium number of cells in a waveform. In Ref. [28] of the main text we showed that the contour of tissue midline is mainly determined by the differential tension  $\alpha - \beta$  and that tissue lateral tension  $\alpha + \beta$  only controls the number of cells in the waveform through the width-to-height ratio; the larger the tissue lateral tension the larger the number of cells in the waveform. The three evaginated folds plotted in Fig. S2 have identical differential tension  $\alpha - \beta = 1.5$  and bending modulus  $\kappa = 0.001$  but they differ in the value of  $\alpha$  ( $\alpha = 0.3$ ,  $\alpha = 0.6$ , and  $\alpha = 1.8$ ) and thus in the value of tissue lateral tension ( $\alpha + \beta = 2.1$ ,  $2.7$ , and  $5.1$ , respectively). As  $\alpha + \beta$  is increased, the number of cells in a waveform clearly increases too whereas the cell width-to-height ratio decreases (Fig. S2B, left column). Nonetheless, the outline of the folds does not change significantly. This is best appreciated by comparing the thick line of fold shapes in the right column of Fig. S2B scaled such that their wavelengths are the same.

At a very low lateral tension  $\alpha + \beta$  where the tissue is squamous,  $\alpha$  and  $\beta > 0$  must be small themselves and so the differential tension is small too. As a result, the tissue is flat. This means that in our model where we

approximate cells as quadrilaterals with flat edges, we cannot obtain nontrivial squamous epithelia.

## B. Apico-basal differential tension

In our model, formation of nontrivial epithelial shapes is driven by the interplay between the spontaneous curvature, determined mainly by the tissue differential tension, and periodic boundary conditions imposed by the implicit (fluid-like) stroma. In case of vanishing basement membrane bending modulus ( $\kappa = 0$ ) the spontaneous curvature of cells describing their preferred shape can be calculated analytically and reads

$$c_0 = -\frac{2\sqrt{\alpha + \beta}(\alpha - \beta)}{[1 - (\alpha - \beta)^2]^{3/4}}. \quad (5)$$

$c_0$  grows with the magnitude of the differential tension  $\alpha - \beta$ , transforming the rectangular shape into a trapezoid and then into a triangle at a threshold of

$$(\alpha - \beta)_{th} = \frac{1}{2} \left[ \alpha + \beta - \sqrt{4 + (\alpha + \beta)^2} \right]. \quad (6)$$

At  $|\alpha - \beta| = (\alpha - \beta)_{th}$  cells are either apically (if  $\alpha > \beta$ ) or basally constricted (if  $\alpha < \beta$ ) and beyond the threshold value cell shape no longer changes with  $\alpha - \beta$ .

Our numerical results show that the differential tension  $\alpha - \beta$  not only determines the tissue spontaneous curvature but also the amplitude of thickness modulation  $\delta l$  in epithelial folds. Here  $\delta l$  is defined as the difference of groove and crest tissue thickness (Fig. 1B of the main text). Figure S3 shows the relative thickness modulation  $\delta l/l_0$  in absence of basement membrane ( $\kappa = 0$ ); here  $l_0 = \sqrt{\alpha + \beta}$  is the leading-order estimate of tissue thickness. In the flat epithelium at  $\alpha - \beta \approx 1.4$ ,  $\delta l/l_0 = 0$  but in the folded epithelium it increases approximately as  $\delta l/l_0 \propto (\alpha - \beta)/\sqrt{\alpha + \beta}$ . Apart from the agreement

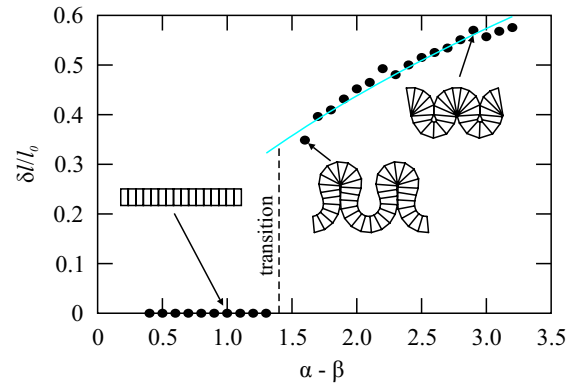


Fig. S3. Relative tissue thickness modulation  $\delta l/l_0$  vs. reduced differential tension  $\alpha - \beta$  in a model epithelium at fixed  $\alpha = 0.6$  and without the basement membrane  $\kappa = 0$ . Insets illustrate a few typical waveforms and in the fold domain at  $\alpha - \beta > 1.4$ ,  $\delta l/l_0 \propto (\alpha - \beta)/\sqrt{\alpha + \beta}$  (cyan line).

with this simple fit, note the large magnitude of relative thickness modulation reaching  $\approx 60\%$  in the tissues shown here. We stress that as the fold shape itself saturates as  $\alpha - \beta$  is increased further (Ref. [28] of the main text) so does  $\delta l/l_0$ , implying that the above approximate formula cannot be generally applicable.

Our results suggest that tissue thickness modulation does not depend very dramatically on the other two parameters of the model, i.e.,  $\kappa$  and  $\alpha + \beta$ . Moreover, they show that for  $\alpha > \beta$  and  $\alpha < \beta$  tissue thickness is largest in the part of the waveform containing apically or basally constricted cells, respectively.

### C. Bending rigidity of basement membrane

As the basement membrane bending modulus  $\kappa$  is increased, the contour of any folded epithelium is somewhat straightened out as seen in Fig. 1D, E of the main text. Unfolding proceeds in two ways depending on the sign of the differential tension (Fig. S4), which can be easily understood by considering a single cell with  $\alpha - \beta > (\alpha - \beta)_{th}$  [Eq. (6)] supported by the basement membrane. If  $\alpha > \beta$  the cell is apically constricted at small  $\kappa$  and the curvature of the basement membrane is small too. As a result, an increase of  $\kappa$  from a infinitesimally small value to a finite value results in a slight unfolding (top row of cells in Fig. S4). On the other hand, if  $\alpha < \beta$  then the cell is basally constricted at small  $\kappa$ , which means that the curvature of the membrane is large (bottom row of cells in Fig. S4). This is associated with a considerable membrane bending energy even with small  $\kappa$  meaning that the tissue unfolds more than in former case at a finite bending modulus.

This behavior is quantified by a dimensionless curvature of cells on the membrane conveniently expressed by the product of cell curvature and height,  $|cl|$ . In Fig. S4,  $|cl|$  is plotted against membrane bending modulus  $\kappa$  for

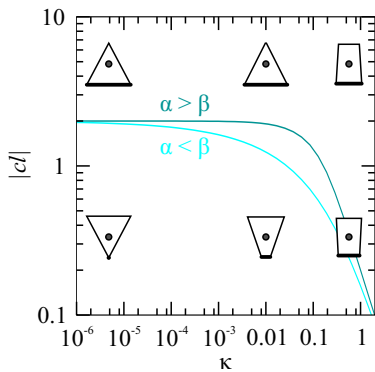


Fig. S4. Product of curvature and height in isolated cells supported by the basement membrane vs. membrane bending rigidity  $\kappa$ . At finite  $\kappa$ , basally constricted cells (cyan line;  $\alpha = 0.6, \beta = 1.07$ ) are unfolded more than the apically constricted cells (dark blue line;  $\alpha = 1.07, \beta = 0.6$ ). Insets show cell shapes at  $\kappa = 0, 0.01$ , and 1.

both  $\alpha > \beta$  and  $\alpha < \beta$  on a log-log scale. At very small  $\kappa$   $|cl| = 2$ , which corresponds to apically constricted triangular cell ( $cl = -2$ ) or basally constricted triangular cell ( $cl = 2$ ). With increasing  $\kappa$ ,  $|cl|$  decreases faster at  $\alpha < \beta$  than at  $\alpha > \beta$ , which means that at small  $\kappa$  basally constricted cells unfold more than the apically constricted cells. The asymptotic behavior of  $|cl|$  for  $\kappa \gg 1$  is identical in both cases.

In Fig. S5 we plot cell curvature and height (i.e., tissue thickness) as a function of differential tension  $\alpha - \beta$  for three values of basement membrane bending modulus. The left panel shows the  $\kappa = 0$  case where the basally constricted cell at a given  $\alpha - \beta < 0$  is equivalent to the apically constricted cell at a positive differential tension of identical magnitude. This is reflected in the symmetry of cell height (cyan line) and in the antisymmetry of curvature (gray line). At a finite  $\kappa$ , the symmetry and the antisymmetry are absent, and at a given magnitude of differential tension  $|\alpha - \beta|$  the apically constricted cells at  $\alpha > \beta$  are more curved and taller than the basally constricted cells at  $\alpha < \beta$ .

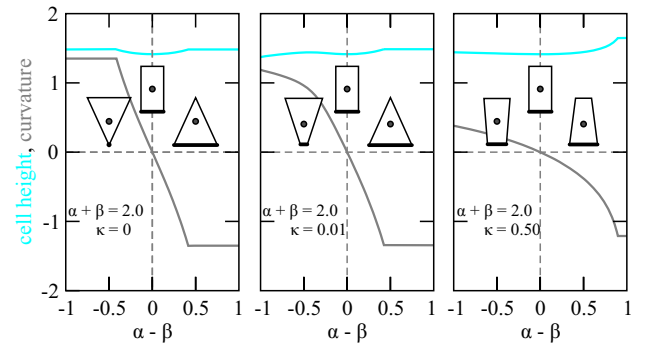


Fig. S5. Curvature and height of a cell supported by the basement membrane of  $\kappa = 0, 0.01$ , and 0.5 (left, middle, and right panel, respectively) plotted vs. differential tension  $\alpha - \beta$ . Also included are shapes of cells at  $\alpha - \beta = -0.5, 0$ , and 0.5.

### D. Cell-cell repulsion

Yet another factor determining fold shape is the repulsion between impenetrable cells represented by a hardcore potential. Each folded morphology can be thought of consisting of two segments. The *favorable* segment contains cells whose shape is very close to that of isolated cells at given  $\alpha, \beta$ , and  $\kappa$  so that their energy is small. On the other hand, cells in the *unfavorable* segment are deformed very much compared to isolated cells at given  $\alpha, \beta$ , and  $\kappa$  and their energy is large. In periodic folds, both favorable and unfavorable segments are needed (Ref. [28] of the main text).

As the differential tension  $\alpha - \beta$  is increased, cells in the unfavorable segment are energetically more and more costly. As a result, in the minimal-energy fold the unfavorable segment consists of as few cells as possible, lead-

ing to sharp grooves and crests (Fig. S6A). In turn, this means that neighboring grooves and crests are physically very close to the point that they actually touch so that non-neighboring cells push against each other (e.g., in waveforms with  $\alpha > 2.5$  in Fig. S6A). At this stage, the contour of the waveform depends on cell-cell repulsion very much and the tissue shape becomes saturated, unable to adapt to a further increase of differential tension. Thus the compact folds are stabilized primarily by apical (or basal) constriction and hard-core cell-cell repulsion whereas the invaginated and evaginated are stabilized mainly by the bending rigidity of the basement membrane and only to a lesser degree by the repulsion between cells (Fig. S6A). In the wavy folds (Fig. 1D, E of the main text) cell-cell repulsion is irrelevant.

Including this constraint in numerical simulations is usually quite a challenge. Here we achieved this as follows: At every minimization step we run the routine which checked whether any two cell overlap. If this was the case, vertices defining both cells in question were forced to a position such that the cells touched rather than overlapped. First, the routine identifies the top and the bottom vertex of the waveform [ $\mathbf{r}_{\text{top}} = (x_{\text{top}}, y_{\text{top}})$  and  $\mathbf{r}_{\text{bott}} = (x_{\text{bott}}, y_{\text{bott}})$ ]. Next, the coordinates  $x_{\text{top}}$  and  $x_{\text{bott}}$  are used as spatial barriers. Cells that were initially on either side of the barrier are not able to cross it. Specifically, for a vertex with coordinates  $\mathbf{r} = (x, y)$  the sign of the quantities  $x - x_{\text{top}}$  and  $x - x_{\text{bott}}$  is forced to remain unchanged during the course of simulation; here  $x_{\text{top}}$  and  $x_{\text{bott}}$  are of course updated at every minimization step.

### E. Stroma

Finally, fold morphologies are only possible in an epithelium supported by a stroma that ensures a global planar nature. Here such a stroma is represented by periodic boundary conditions mimicking, e.g., an epithelium floating on a fluid-like substrate. Such a substrate can be viewed as an idealization of a small part of a droplet (Fig. S7) corresponding, e.g., to yolk in a *Drosophila* embryo without the vitelline membrane as discussed in Ref. [27] of the main text.

## II. PHASE DIAGRAM OF FOLD MORPHOLOGIES

The waveforms shown in Fig. 1D, E of the main text are just a representative subset of all waveforms that we obtained. A more comprehensive selection is presented in Fig. S8, panels A and B corresponding to those in Fig. 1D and E of the main text. Figure S8 illustrates two important facts: (i) the continuous deformation of any given shape as either apical or basal tension and the basement membrane bending rigidity are varied, and (ii) the uneven sensitivity of waveforms to these parameters

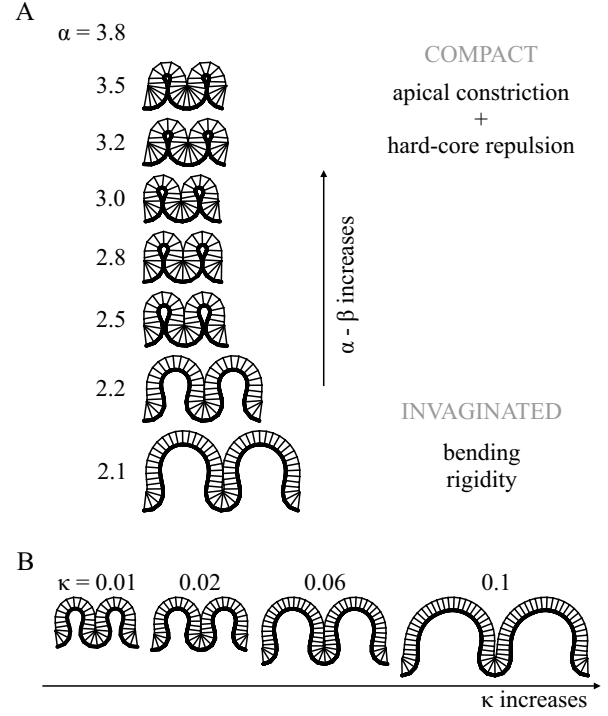


Fig. S6. Comparison of compact and invaginated folds at  $\beta = 0.6$  and  $\kappa = 0.02$  and various  $\alpha$  (panel A). The shape of the former is determined mainly by apical constriction of groove cells and by the cell-cell repulsion whereas the latter are stabilized primarily by the basement membrane. Panel B shows a sequence of waveforms at  $\alpha = 2.2$  and  $\beta = 0.6$  as  $\kappa$  is increased, illustrating the ever less important role of cell-cell repulsion.

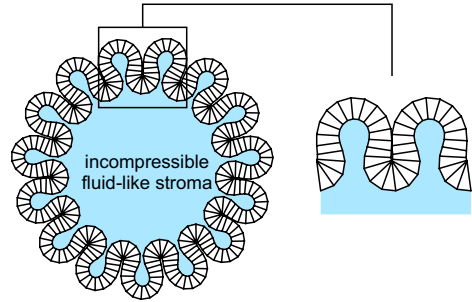


Fig. S7. Folded 2D model epithelium around an incompressible droplet of fixed area (blue). The model explored in this study can be viewed as a small part of such an epithelium.

across the phase diagram.

The leftmost columns of the two panels of Fig. S8 contain shapes at vanishing bending rigidity of the basement membrane ( $\kappa = 0$ ). As a result, a shape with a given apical and basal tension  $\alpha_A = 0.6$  and  $\beta_A$  in panel A is a mirror image of its counterpart with  $\alpha_B = \beta_A$  and  $\beta_B = 0.6$  in panel B; as the waveforms are plotted in a crest-to-crest fashion, a half-wavelength horizontal shift is needed to appreciate the correspondence. In the regime of compact folds at large differential tension (e.g., at  $\beta \gtrsim 2.5$

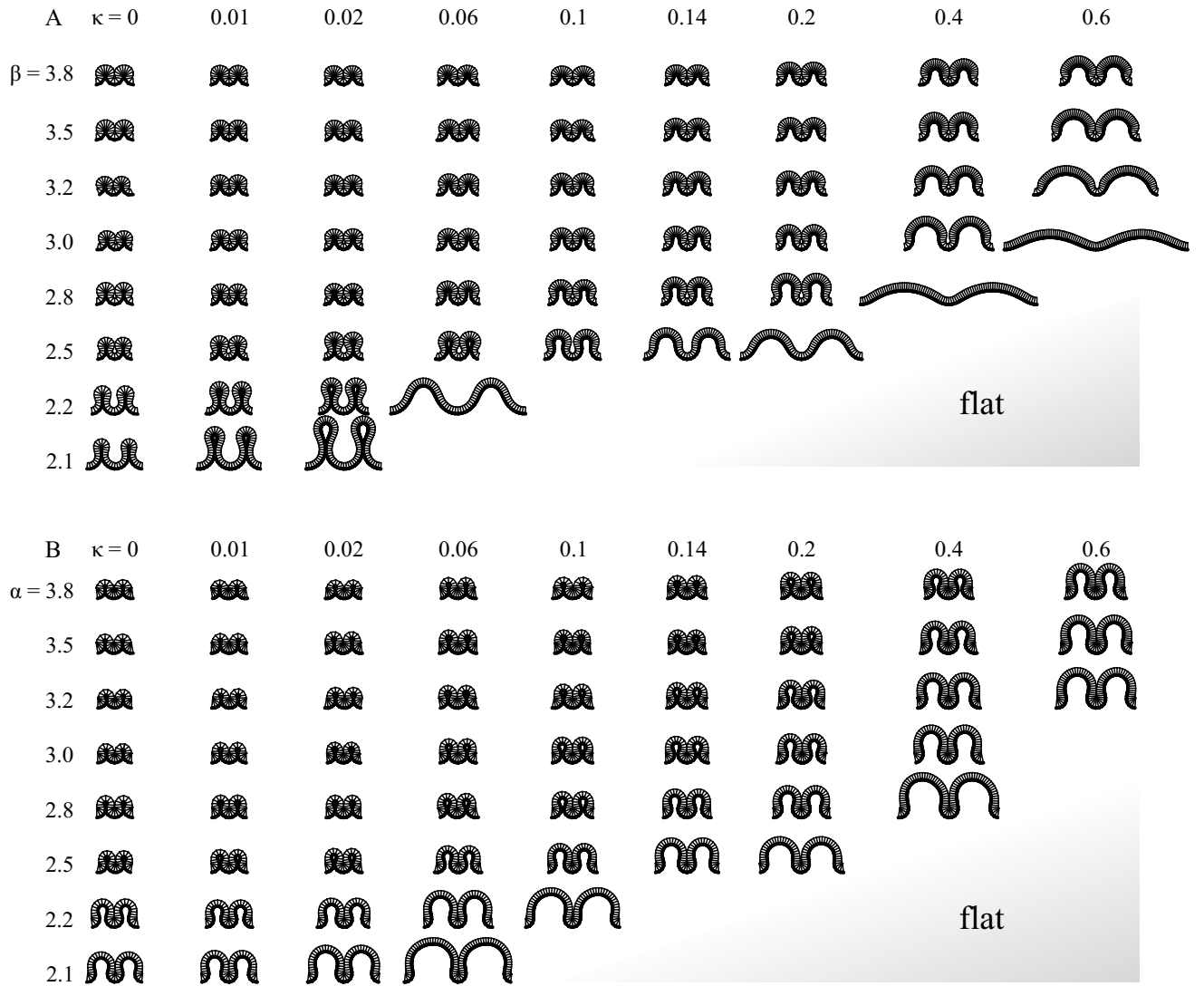


Fig. S8. Selected fold morphologies for  $\alpha < \beta$  (A) and  $\alpha > \beta$  (B). In panel A  $\alpha = 0.6$  and in panel B  $\beta = 0.6$ ; note that neither the bending modulus of the membrane (columns) nor the basal and apical tension (rows) is equidistant. Flat epithelia are stable at large  $\kappa$  and small  $\beta$  and  $\alpha$ , respectively, as sketched by the shaded regions.

in panel A and  $\alpha \gtrsim 2.5$  in panel B) the folds are tightly packed and rather symmetric about the horizontal, but at intermediate differential tensions the difference between the evaginated folds with basally constricted cells in the crests in panel A and the corresponding invaginated folds with apically constricted cells in the grooves in panel B is clear.

At finite  $\kappa$ , this symmetry is broken because the bending rigidity of the basement membrane prevents basal constrictions of the folds with in Fig. S8A because it is located at the basal side. On the other hand, waveforms in Fig. S8B may contain a certain fraction of apically constricted cells, which are located in the grooves. This asymmetry is clearly seen in the generally larger wavelength of any given fold in panel A compared to its counterpart in panel B, the most extreme manifestation of this effect being the wavy folds in panel A.

Another consequence of the basement membrane is the small range of  $\kappa$  where evaginated folds are stable. As evident from the waveforms in the bottom rows of both panels in Fig. S8, the basement membrane permits deep and sharp invaginations within a broad range of  $\kappa$  provided that the differential tension is suitable (as seen, e.g., in the  $\alpha = 2.8, \kappa = 0.4$  in panel B) but tall evaginations are only possible at very small  $\kappa$  (cf. waveform  $\beta = 2.1, \kappa = 0.02$  in panel A). Thus a sharp evagination can be viewed as a signature of a small bending rigidity of the basement membrane.

Apart from the wavelength, the main difference between folds with  $\alpha < \beta$  in Fig. S8A and those with  $\alpha > \beta$  in Fig. S8B is the relative tissue thickness in grooves and in crests. In waveforms in panel A, crest cells are taller than those in the grooves, and the grooves are incompletely closed or even open (the most extreme case be-

ing the wavy folds). Waveforms in panel *B* have crests which consist of trapezoidal cells shorter than cells in the grooves, which are apically constricted; as a result, the grooves are closed.

Some waveforms in Fig. S8 apparently consist of very simple geometric shapes. The contour of the meandering evaginated shape shown in Fig. 9A can be approximated by circular arcs of two radii, and the midline of the wavy fold in Fig. 9B is almost sine-like.

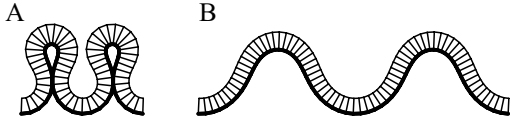


Fig. S9. Meandering evaginated fold (*A*;  $\alpha = 0.6, \beta = 2.2$ , and  $\kappa = 0.02$ ), and sine-like wavy fold (*B*;  $\alpha = 0.6, \beta = 2.2$ , and  $\kappa = 0.06$ ).

Figure 1*D, E* of the main text zooms in the region of the phase diagram where the differential tension is large enough so as to stabilize fold morphologies yet not too big so as to induce the reentrant fold-flat transition explored in detail in Ref. [28] of the main text. In Fig. S10, we sketch the **global topology of the phase diagram** which does contain this transition. As any finite bending rigidity of the basement membrane disfavors fold morphologies compared to either thin and the thick flat epithelium stable at small and large differential tensions, respectively, we expect that the fold region in the phase diagram should gradually shrink as  $\kappa$  is increased and that there exists a critical bending rigidity of the basement membrane  $\kappa_c$  beyond which the epithelium is flat at any  $\alpha$  and  $\beta$ .

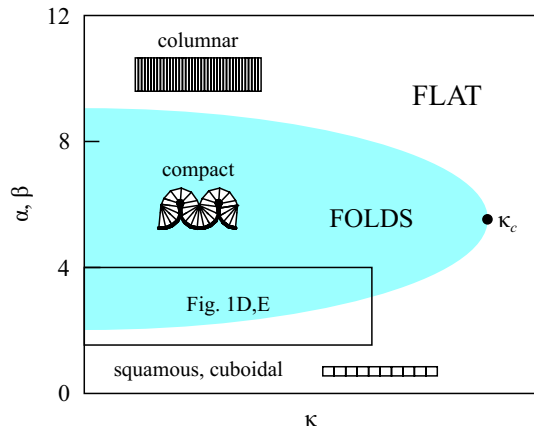


Fig. S10. Global topology of the phase diagram of fold morphologies with the reentrant flat-fold-flat morphological sequence at bending rigidities smaller than the critical value of  $\kappa_c$ . Also indicated semiquantitatively is the domain explored in Fig. 1*D, E* of the main text.

### III. PHYSIOLOGICAL FUNCTION OF EPITHELIAL FOLDS

Monolayered epithelial sheets cover body surfaces of invertebrates and luminal surfaces of most vertebrate internal organs. Epithelial sheets with a free surface are polarized and form barriers which (i) control the passage of matter and provide (ii) protection from mechanical damage and (iii) invasion by different organisms or particles. The barrier function of epithelia depends on close lateral attachments of the cells. The shape and the distribution of cells in epithelial folds varies among the four fold types, and here we discuss the biological relevance of each type in relation to organ function and dynamics.

**Compact folds** with large basal tension are present in the wing imaginal disc of *Drosophila melanogaster* larva (Fig. 3*A\** of the main text). Imaginal discs in holometabolous insect larva are small sacs of concentrated epithelial folds, fated to differentiate into the epidermal structures of the adult during metamorphosis. During imaginal disc formation, considerable epithelial growth and folding takes place in the small area of the sac. Folds are placed tightly close to each other (so that their wavelength is short) and most cells are constricted. Compact folds are also observed in some areas of bronchus (Fig. 3*A\*\** of the main text). Lung bronchi are the conducting part of respiratory system, functioning in air passage and in conditioning of the air with mucus covering the internal surface of bronchi. The bronchus epithelial folds serve to increase surface area for mucus secretion and enable changing of airway diameter, which is achieved by differential epithelial folding with compact regions.

The folded intestinal epithelium is the site for digestion and absorption of food. **Invaginated folds** of the intestine epithelium in bony fishes increase the digestive and absorptive surface area (Fig. 3*B\** of the main text). In mammal colon (Fig. 3*B\*\** of the main text) the epithelium surface is increased by folds for effective resorption of electrolytes and water as well as for secretion of mucus. Both epithelia represent the invaginated fold type with  $\alpha > \beta$  and they consist primarily of absorptive cells. The trapezoidal cells with wide apical surfaces located in the crests are shorter and wider than cells in the grooves which are constricted apically and enlarged basally. This type of epithelium functions primarily in absorption and fluid transport.

**Invaginated folds** with  $\alpha < \beta$  are identified in actinopharynx of cnidarians, serving as the organ of water flow and food transport (Fig. 3*C\** of the main text) and in vertebrate bronchiole, functioning in air conduction and lipoprotein secretion (Figs. 3*C\*\** and 3*C\*\*\** of the main text). In these folds, cells in the crests are basally constricted and are taller and more numerous than those located in the grooves. Grooves are wider than in the invaginated epithelium with  $\alpha > \beta$  (Figs. 3*B\** and 3*B\*\** of the main text). This type of epithelium functions primarily in secretion and in air, fluid or food

transport. Basally constricted crest cells may increase secretory activity by releasing packages of secretory vesicles with lipoprotein to prevent collapsing of bronchioles.

In a **wavy fold**, the wavelength is much larger than the amplitude. This type of epithelial folds is found at the body surface of snail *Helix sp.* (Fig. 3D\* of the main text) covered by mucus-secreting epidermis. Folds increase the surface area for secretion and allow extension of body surface. The apical surfaces of epidermal cells remain fully exposed to the exterior in the crests as well as in the grooves. Wavy epithelial folds are also present in the hindgut of earthworm *Lumbricus sp.* (Fig. 3D\*\* of the main text), functioning in resorption of water, osmoregulation, and feces formation. In vertebrate bronchiole (Fig. 3D\*\*\* of the main text) the wavy epithelium functions in air conduction and lipoprotein secretion. The fold-to-fold variability observed in histological sections reflect the dynamics of epithelial folds related to changes of lumen diameter and secretion.

Folds in the **evaginated epithelium** display wide grooves and basally constricted cells in crests which are slightly higher than cells in grooves. Evaginated folds are identified in bronchiole of cat lung (Fig. 3E\* of the main text) providing air conduction. Here the folds enable lumen to expand when air or food passes through it. Evaginated epithelial folds are also found in mammal oviduct (Fig. 3E\*\* of the main text) with bidirectional transport of the gametes and secreted fluids. The longitudinal folds in the intestine of trout (Fig. 3E\*\*\* of the main text) increases the digestive and absorptive surface area and the distinct grooves in between the folds serve in the retention of ingested food for longer periods and in nutrition passage.

#### IV. APPARENT DISTORTION OF FOLDS IN HISTOLOGICAL SECTIONS

None of the histological sections presented in Fig. 3 of the main text was prepared specifically for morphometrical purposes related to our theoretical findings. Instead, the sections were chosen based on qualitative agreement of the folds that they contain with our theoretical predictions summarized in Fig. S8. While studying the published sections and our own archive, we did bear in mind that the sections may not show a given morphology as representatively as possible partly due to purely geometrical reasons related to the direction of the cut while slicing the sample.

Ideally, a fold epithelium would be cut along a plane perpendicular to grooves and crests. Sectioning it at a non-ideal angle distorts the representative cross-section and thus biases the measured absolute and relative modulation of tissue curvature  $c$  and thickness  $l$  as key parameters of fold morphologies. For each theoretical fold contour, the distortion can be quantified semi-analytically as follows. We first approximate the exact contour by a two interpolating functions  $\mathcal{A}(x)$  and  $\mathcal{B}(x)$  representing

the apical and the basal side of the tissue, respectively. [Here we tacitly assume that there are no overhangs in the folds so that both  $\mathcal{A}(x)$  and  $\mathcal{B}(x)$  depend on a single coordinate  $x$ ; see Fig. S11. In case of overhangs, a more general representation is needed.] In a parametric form the apical and basal surface are thus fully described by  $\mathbf{r}_a = (x, y, \mathcal{A}(x))^T$  and  $\mathbf{r}_b = (x, y, \mathcal{B}(x))^T$ , respectively, where the  $y$  axis points along the folds.

Cutting these surfaces in any plane given by  $y = y_0$  produces a representative cross-section but rotating the cut plane does not. Here this effect is quantified by rotating the apical and basal surface relative to the cut plane, that is, about the  $x$  and the  $z$  axis by angles  $X$  and  $Z$ , respectively. These rotations are represented by matrices

$$\mathbf{R}_x(X) = \begin{pmatrix} 1 & 0 & 0 \\ 0 & \cos X & -\sin X \\ 0 & \sin X & \cos X \end{pmatrix} \quad (7)$$

and

$$\mathbf{R}_z(Z) = \begin{pmatrix} \cos Z & -\sin Z & 0 \\ \sin Z & \cos Z & 0 \\ 0 & 0 & 1 \end{pmatrix}, \quad (8)$$

After both rotations, the apical surface after the rotation around both axes is transformed to

$$\begin{aligned} \mathbf{r}'_a &= (x'_a, y'_a, z'_a)^T = \mathbf{R}_x(X)\mathbf{R}_z(Z)\mathbf{r}_a \\ &= \begin{pmatrix} x \cos Z - y \sin Z \\ -\mathcal{A}(x) \sin X + \cos X(y \cos Z + x \sin Z) \\ \mathcal{A}(x) \cos X + \sin X(y \cos Z + x \sin Z) \end{pmatrix} \end{aligned} \quad (9)$$

In the cut plane  $y'_a = y_0$  which means that

$$y = [y_0 + \mathcal{A}(x) \sin X]/(\cos X \cos Z) - x \tan Z \quad (10)$$

and after a few final straightforward steps we obtain

$$\mathbf{r}'_a = \begin{pmatrix} x/\cos Z - [y_0 + \mathcal{A}(x) \sin X] \tan Z/\cos X \\ y_0 \\ [\mathcal{A}(x) + y_0 \sin X]/\cos X \end{pmatrix} \quad (11)$$

The results for the coordinates of a point at the basal surface are analogous. Without loss of generality we can set  $y_0 = 0$  and plot the parametric curves  $(x'_a(x), z'_a(x))$  and  $(x'_b(x), z'_b(x))$  representing the apical and the basal side, respectively.

Figure S11A shows the representative cross-section of the folds, the black, dark blue, and cyan arrow indicating the true wavelength  $\lambda$  as well as groove and crest thicknesses  $l_g$  and  $l_c$ , respectively. If the cut plane is tilted about the  $x$  axis (Fig. S11B; here  $X = 36^\circ$ ) the groove and the crest thicknesses are apparently increased as seen by comparing the true  $l_g$  and  $l_c$  (dark blue and cyan arrow, respectively) with the contour. The wavelength remains unchanged. Rotating the cut plane about the  $z$  axis leaves the groove and crest thicknesses unaltered but leads to an apparent increase of the wavelength (Fig. S11C; here  $Z = 36^\circ$ ). Finally, simultaneous tilt

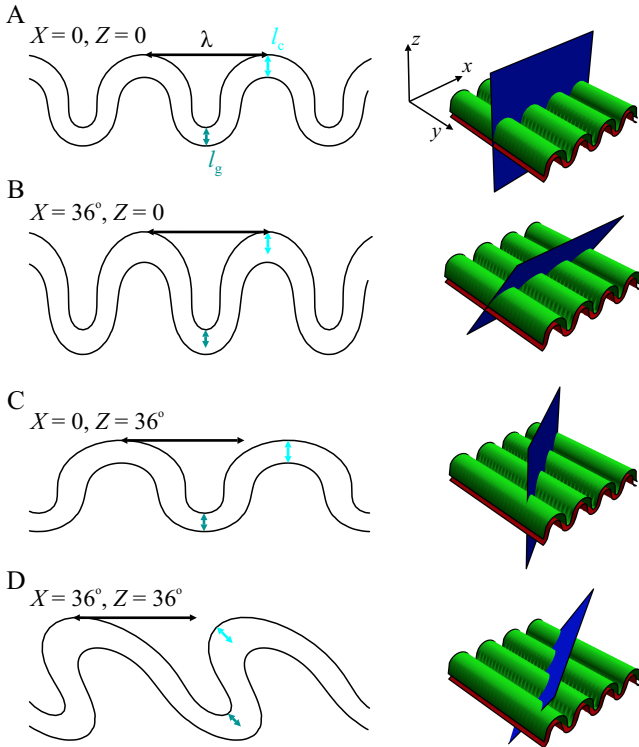


Fig. S11. Geometrical distortion of the folds caused by misalignment of the cut plane. The representative fold contour is seen in a section perpendicular to the direction of the grooves (A, arrows indicate groove and crest tissue thickness and fold wavelength). Tilting the cut plane does not affect the fold wavelength but the apparent groove and crest tissue thicknesses are increased (B); rotating it about the  $z$  axis pointing into lumen leaves the thickness unchanged but increases the wavelength (C). A combination of tilt and rotation leads to tilted folds and an apparent increase of  $l_g$ ,  $l_c$ , and  $\lambda$  (D).

about the  $x$  axis and rotation about the  $z$  axis result in a combined distortion of the cross-section seen in Fig. S11D for  $X = 36^\circ$  and  $Z = 36^\circ$ . In this case, the folds themselves are tilted rather than upright and they are not symmetric,  $\lambda$ ,  $l_g$ , and  $l_c$  and all are apparently increased. Moreover, the true bottom of the groove and the true top of the crest are both displaced as indicated by the dark blue and the cyan arrow, respectively. Interpreting the apparent groove and crest thicknesses measured at the top and the bottom of the tilted and rotated section may thus be challenging.

An additional effect potentially leading to a larger error are the often poorly visible cell boundaries, which make measurements of tissue thickness even more difficult. Within our model, cells are perpendicular to tissue cross-section midline but in a tilted and histological section this may no longer hold. Thus the apparent tissue thickness measures as the perpendicular distance between the apical and the basal surface is generally different from the true distance.

We expect that in most histological sections, the ori-

entation of the cut plane is somewhat imperfect, with tilt and rotation angles of up to 10 or 15° being acceptable. In addition, the epithelium itself is almost never ideally periodic. The direction of grooves themselves may vary so that a given histological section may be representative in a part of the sample but not across all of it. These considerations must be taken into account when interpreting the sections, and it is possible that they are responsible for some fold-to-fold variability seen in Fig. 3A\*-E\*\*\* of the main text.

Finally, we note that seeing a continuous albeit distorted folds in a non-representative histological section is also a strong indication that the epithelium in question indeed has longitudinal folds and not villi. Irrespective of the orientation of the cut plane, folds should always appear as a continuous contour but in case of villi one may either see a representative lengthwise cross-section or just a disconnected circular patch as in Fig. 4f in Ref. [1]. In addition, the spacing of the folds seen in Fig. 3A\*-E\*\*\* of the main text is still very regular and well-defined whereas in villi it need not appear to be regular because of a misaligned cut plane even in fairly ordered villi patterns such as the hexagonal and the square lattice of the colon and the intestinal villi, respectively (Ref. [5] of the main text). An oblique-view electron micrograph of the epithelium such as that in Fig. 1A of the main text is even more convincing but seldom available.

## V. MODEL PARAMETERS

The model parameters of the theoretical epithelial folds overlaid onto histological sections in Fig. 3A\*-E\*\*\* of the main text are summarized in Table SI. Note that as far as fold shape is concerned, the only meaningful parameters are the reduced differential tension  $\alpha - \beta$  and bending rigidity  $\kappa$ . As mentioned in the main text, varying  $\alpha$  and  $\beta$  at fixed  $\alpha - \beta$  and  $\kappa$  merely affects cell height-to-width ratio but not the shape of the waveform.

Table SI. Model parameters of the theoretical folds shown in panels A\*-E\*\*\* of Fig. 3 of the main text.

tissue	$\alpha$	$\beta$	$\alpha - \beta$	$\kappa$
fruit fly wing imaginal disc, A*	0.6	2.8	-2.2	0.01
cat lung bronchus, A**	0.6	2.8	-2.2	0.01
silver sailfin molly intestine, B*	2.1	0.6	1.5	0.02
rat small intestine, B**	3.8	0.6	3.2	0.4
metridium actinopharynx, C*	0.6	2.8	-2.2	0.14
cow bronchus, C**	0.6	2.5	-1.9	0.1
mouse bronchiole, C***	0.6	2.5	-1.9	0.1
snail body surface, D*	0.6	3.2	-2.6	0.6
earthworm hindgut, D**	0.6	2.8	-2.2	0.4
mouse bronchiole, D***	0.6	2.8	-2.2	0.3
cat lung bronchus, E*	0.6	2.1	-1.5	0.002
monkey oviduct, E**	0.6	2.1	-1.5	0.002
trout intestine, E***	0.6	2.3	-1.7	0

- 
- [1] Yao J, Maslov KI, Puckett ER, Rowland KJ, Warner BW, Wang LV (2012) Double-illumination photoacoustic microscopy. *Opt Lett* 37:659-661.